

RB-SCD: A New Benchmark for Semantic Change Detection of Roads and Bridges in Traffic Scenes

Qingling Shu, Sibao Chen*, Zhihui You, Wei Lu, Jin Tang and Bin Luo

MOE Key Lab of ICSP, IMIS Lab of Anhui Province, Anhui Provincial Key Lab of Multimodal Cognitive Computation, School of Computer Science and Technology, Anhui University, Hefei, China

ARTICLE INFO

Keywords:

Change detection
Road and bridge semantic change detection dataset
Dynamic frequency coupler
Textual frequency filter

ABSTRACT

Accurate detection of changes in roads and bridges, such as construction, renovation, and demolition, is essential for urban planning and traffic management. However, existing methods often struggle to extract fine-grained semantic change information due to the lack of high-quality annotated datasets in traffic scenarios. To address this, we introduce the Road and Bridge Semantic Change Detection (RB-SCD) dataset, a comprehensive benchmark comprising 260 pairs of high-resolution remote sensing images from diverse cities and countries. RB-SCD captures 11 types of semantic changes across varied road and bridge structures, enabling detailed structural and functional analysis. Building on this dataset, we propose a novel framework, Multimodal Frequency-Driven Change Detector (MFDCD), which integrates multimodal features in the frequency domain. MFDCD includes a Dynamic Frequency Coupler (DFC) that fuses hierarchical visual features with wavelet-based frequency components, and a Textual Frequency Filter (TFF) that transforms CLIP-derived textual features into the frequency domain and applies graph-based filtering. Experimental results on RB-SCD and three public benchmarks demonstrate the effectiveness of our approach.

1. Introduction

In the field of remote sensing (RS), change detection (CD) has become an essential task for monitoring environmental, urban, and infrastructure changes (Pekel et al., 2016; Song et al., 2018). With the acceleration of urbanization and the continuous development of transportation infrastructure, CD in traffic scenes is crucial for traffic planning and facility management. In traffic planning, accurately identifying structural and functional changes in roads and bridges helps urban authorities to assess the current state of transportation networks, forecast future demands, and make data-driven decisions about expansions, detours, and upgrades (Lin and Habib, 2022; K S et al., 2024; Wang et al., 2025). For instance, the emergence of new overpasses, flyovers, or road expansions needs to be timely integrated into transportation maps to ensure up-to-date routing and navigation services. Moreover, detecting illegal road constructions or temporary blockages is also critical for enforcing urban regulations and minimizing congestion. From the perspective of traffic facility management, road and bridge CD enables timely identification of structural deterioration, unauthorized demolitions, or unreported construction activities. This semantic-level understanding is crucial for preventive maintenance, disaster response (e.g., after floods or earthquakes), and resource allocation. Additionally, as smart cities and autonomous transportation systems increasingly rely on accurate and up-to-date digital maps, the need for automated and fine-grained CD becomes even more pressing. Roads and bridges are not only physical assets but also key elements in the digital infrastructure of intelligent transportation systems.

However, as shown in Table 1, traditional binary change

detection (BCD) datasets (Ji et al., 2018; Chen and Shi, 2020; Shi et al., 2021), etc. primarily focus on building CD and only provide simple information about whether a change has occurred, represented by 0 and 1 for no change and change, respectively. On the other hand, existing semantic change detection (SCD) datasets (Caye Daudt et al., 2019; Yuan et al., 2022; Yang et al., 2022a), etc. mainly focus on changes in land cover, such as building changes and vegetation changes. Changes related to roads and bridges in traffic scenes are either limited in number or completely absent. To address this issue, as annotation examples shown in Figure 1, we propose a new dataset specifically designed for SCD of roads and bridges in traffic scenes: **Road and Bridge Semantic Change Detection (RB-SCD)** dataset. RB-SCD provides semantic annotations for 11 distinct categories of road and bridge changes, effectively addressing insufficient granularity of information and lack of specificity in detecting road and bridge changes in traffic scenes.

In addition to the RB-SCD dataset, we have also developed a new framework to further facilitate CD performance, the **Multimodal Frequency-Driven Change Detector (MFDCD)**, which integrates multimodal features in the frequency domain. Considering CD methods, traditional approaches often rely on convolutional neural network architectures (Caye Daudt et al., 2018; Fang et al., 2022; Feng et al., 2022), which are insufficient to fully exploit the rich spatiotemporal information in images. Some studies (Chen et al., 2022; Bandara and Patel, 2022; Feng et al., 2023) have incorporated transformers into the network for global modeling. However, these methods still face challenges in accurately capturing and effectively distinguishing complex textures and structural changes. Research has also shown that relying solely on single-modal data has inherent limitations. Recently, some methods (Yang et al., 2022b; Zhang et al., 2023; Dong et al., 2024) have introduced multimodal

*Corresponding author

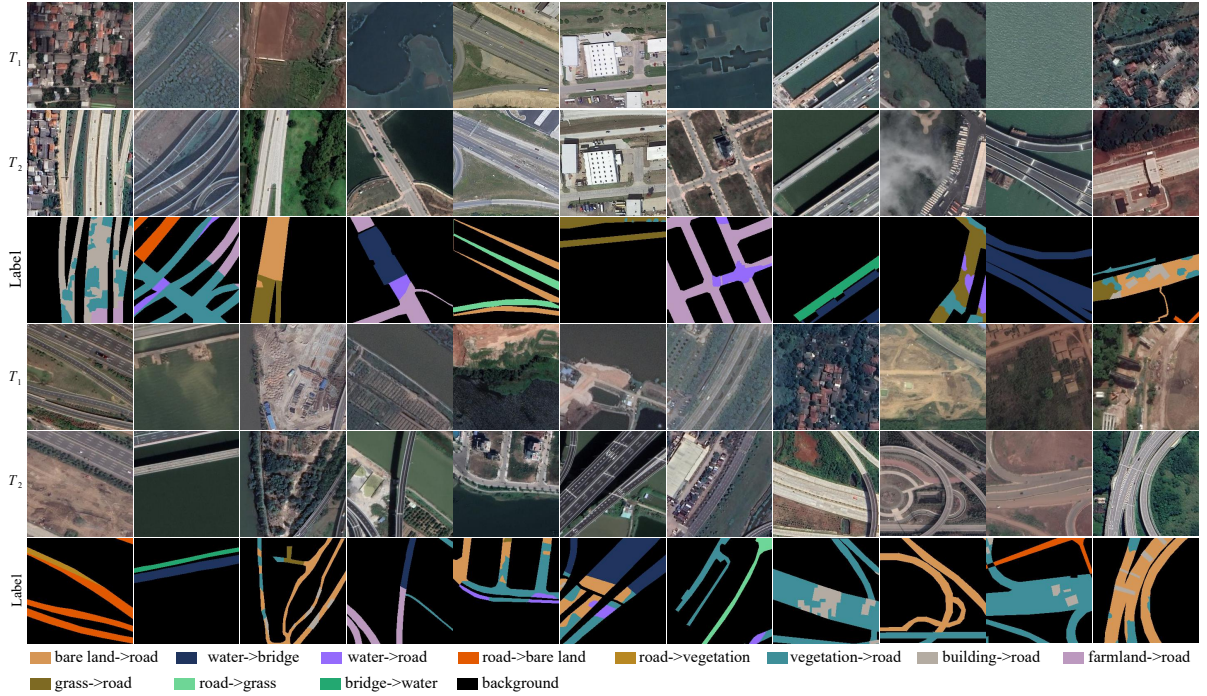
✉ sq1@stu.ahu.edu.cn (Q. Shu)

ORCID(s): 0009-0003-1868-4498 (Q. Shu)

Table 1

The public datasets for urban change detection with optical remote sensing imagery.

Dataset	Resolution (m)	Image pairs	Image size (pixels)	Change type	Objects of interest	Classes
LMR (Low-to-Medium Resolution)						
OSCD (Daudt et al., 2018)	10	24	600×600	Binary	Land cover	–
S2MLTCP (Leenstra et al., 2021)	10	1520	600×600	Binary	Land cover	–
ZY3 (Zhang and Shi, 2020)	5.8	1	1154×740	Binary	Land cover	–
Landsat-SCD (Yuan et al., 2022)	30	8468	416×416	Semantic	Land cover	4
HR (High-Resolution)						
WV3 (Zhang and Shi, 2020)	2	2	1431×1431	Binary	Land cover	–
QB (Zhang and Shi, 2020)	2.4	1	1154×740	Binary	Land cover	–
VHR (Very High-Resolution)						
AICD (Bourdis et al., 2011)	0.5	1000	800×600	Binary	Land cover	–
LEVIR-CD (Chen and Shi, 2020)	0.5	637	1024×1024	Binary	Buildings	–
WHU (Ji et al., 2018)	0.2	1	32207×15354	Binary	Buildings	–
CDD (Lebedev et al., 2018)	0.03 - 1	16000	256×256	Binary	Buildings	–
SYSU (Shi et al., 2021)	0.5	16000	256×256	Binary	Buildings	–
BDD (Adriano et al., 2021)	1.0	1147	250×250	Semantic	Buildings	1
HRSCD (Caye Daudt et al., 2019)	0.5	291	10000×10000	Semantic	Land cover	5
SECOND (Yang et al., 2022a)	0.5 - 3	4662	512×512	Semantic	Land cover	6
Hi-UCD (Tian et al., 2020)	0.1	1293	1024×1024	Semantic	Land cover	9
RB-SCD (Ours)	0.59	260	$270 \times 534 - 7215 \times 4366$	Semantic	Roads and bridges	8

**Figure 1:** Annotation examples on RB-SCD dataset. T_1 and T_2 represents pre- and post-change images, respectively.

features to overcome the shortcomings of single modalities, such as combining visual and textual information or integrating lidar and hyperspectral data. However, these approaches often fail to fully exploit the characteristics of multimodal features, focusing only on modeling the commonalities of multimodal data while neglecting the distributional differences among different modalities.

In this work, as shown in Figure 2, we observe that the decomposition and utilization of features in the frequency domain remain underexplored, particularly the fine-grained

change information embedded in the high-frequency visual features, the large-scale distribution information in the low-frequency features, and the frequency-domain representation of textual features. The potential patterns of multimodal information in the frequency domain have not been adequately studied. Therefore, we make the first attempt to develop a new architecture that maps image and textual features into different types of frequency domains based on their characteristics, enabling multimodal frequency-domain modeling for CD.

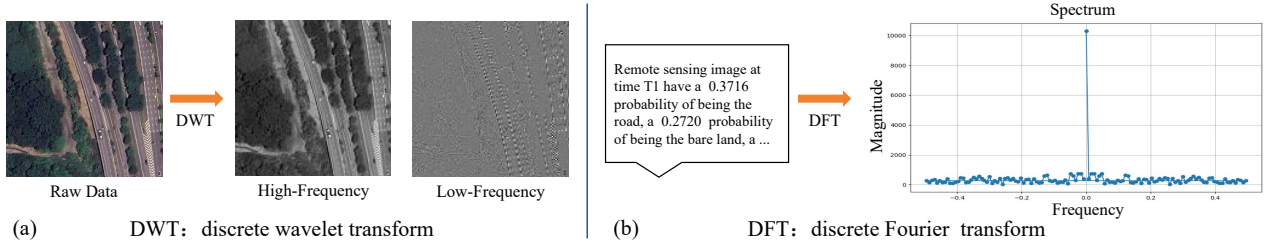


Figure 2: Visualization of visual and textual frequency spectrum.

Our MFDCD consists of two main components: **Dynamic Frequency Coupler (DFC)** and the **Textual Frequency Filter (TFF)**. DFC decomposes bi-temporal features into high- and low-frequency components using discrete wavelet transform (DWT), and introduces an **Adaptive Sparse Frequency Fusion (ASFF)** block for the combination of high-frequency information and low-level features. During the early stages of training, ASFF enhances the sparsity of high-frequency features, focusing on significant change areas. In the later stages, the sparsity constraint is reduced to enhance the expressive power of the model, ultimately increasing the attention to key change areas while suppressing high-frequency noise interference. In this way, edge and texture information in low-level features can not only be gradually captured through convolution operations but also dynamically weighted based on the localized changes in refined high-frequency information. For low-frequency features, **Bidirectional Temporal Frequency Fusion (BTFF)** block is introduced. Since CD involves not only capturing local changes but also understanding the relative changes between different time points, simply combining the high-level features at a single time point with low-frequency features could cause the model to overly rely on the local structural information at that moment, neglecting the cross-temporal changes. The BTFF block addresses this by combining high-level features with low-frequency features across time points, enabling the model to understand the trend of changes and global structural changes over time.

TFF introduces a pre-trained CLIP (Radford et al., 2021) model to obtain textual information, which is further expanded to get text descriptors. Text features contain semantic information but lack spatial features, and discrete Fourier transform (DFT) can convert them into frequency domain information, making it easier to align with the frequency information of image features. By constructing graph filters to aggregate key information, the processed textual features are deeply integrated with visual features to provide multimodal support for SCD.

Our contributions are as follows:

- **A comprehensive benchmark for SCD in traffic scenarios.** We construct a new dataset named RB-SCD, which focuses on SCD of roads and bridges. It contains 260 large-scale high-resolution RS image pairs, covering over ten cities across multiple countries and annotating 11 typical semantic change types. With its wide geographic diversity and complex traffic infrastructures,

RB-SCD supports fine-grained structural and functional change analysis for transportation environments.

- **A novel multimodal frequency-driven CD framework.** We propose Multimodal Frequency-Driven Change Detector (MFDCD), the first framework to introduce frequency-domain multimodal feature integration for CD. It consists of two main modules: (1) Dynamic Frequency Coupler (DFC), which fuses hierarchical visual features with high- and low-frequency components obtained via wavelet transform to enhance cross-temporal structural change perception; (2) Textual Frequency Filter (TFF), which transforms textual features extracted by a pre-trained CLIP model into the frequency domain using Fourier transform, applies graph-based filtering to extract salient components, and integrates them with visual features for collaborative multimodal representation learning.

- **Comprehensive experiments on multiple benchmarks.** Extensive experiments on the proposed RB-SCD and three public CD datasets demonstrate that MFDCD achieves superior performance and generalization ability in identifying complex semantic changes in traffic scenes.

2. Related Work

2.1. CD Datasets and Methods

Existing datasets, as shown in Table 1, such as (Ji et al., 2018; Lebedev et al., 2018; Chen and Shi, 2020; Shi et al., 2021), are primarily designed for BCD tasks and cannot provide specific semantic change information. For SCD, datasets like (Caye Daudt et al., 2019; Yuan et al., 2022; Yang et al., 2022a) have established some benchmarks. However, these datasets mainly focus on changes in land cover, with little attention paid to the changes in roads and bridges in traffic scenes. In contrast, our RB-SCD dataset is a high-resolution, fine-grained SCD dataset specifically curated and annotated for road and bridge changes in traffic scenes. It captures a wide range of semantic change types and includes diverse geographical contexts, enabling precise and meaningful evaluation of CD algorithms in real-world urban transportation scenarios. By addressing both the lack of semantic detail and the absence of domain specificity in existing datasets, RB-SCD provides a valuable and targeted benchmark for infrastructure monitoring, intelligent transportation analysis, and traffic scene understanding.

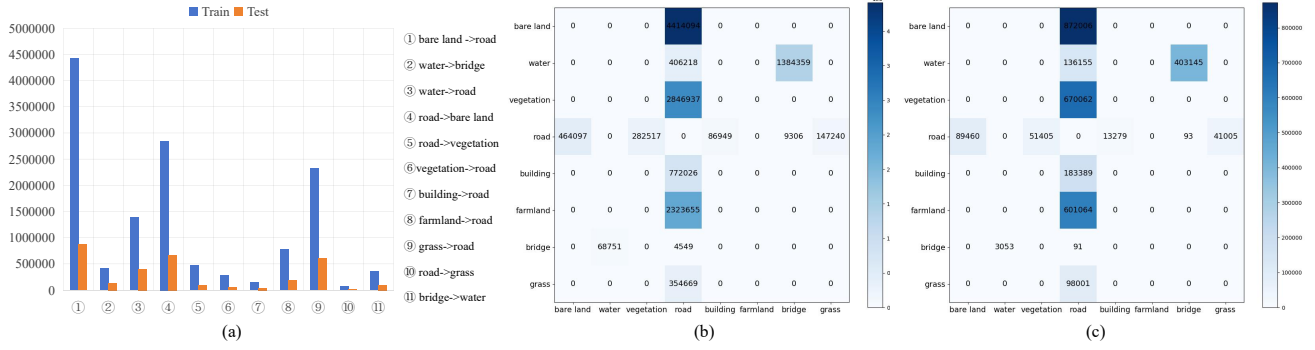


Figure 3: (a) Statistical distribution of pixels for semantic change categories. (b) Train set. (c) Test set.

Table 2
Specific subcategories in RB-SCD dataset.

Categories	Description
Road	street, highway, dirt road, walkway, railway, etc
Bridge	beam bridge, arch bridge, cable-stayed bridge, suspension bridge, etc.
Bare land	wasteland, sand patches area, unpaved open grounds, road or railway construction zones, etc.
Grass	urban lawn, green belt, wetland grass, riparian grass zone, meadow etc.
Water	ocean, lake, river, reservoir, pond, etc.
Farmland	agricultural land (with and without crops)
Vegetation	forest, shrub, urban vegetation buffer, etc.
Building	residential building, commercial building, industrial building, under-construction building (with clear structure), etc.

In recent years, deep learning has significantly improved the accuracy of CD through its ability to extract relevant features from raw data. Changemask (Zheng et al., 2022) decouples SCD into temporal semantic segmentation and BCD, and combines these two tasks into a unified encoder-transformer-decoder framework. MDENet (Liu et al., 2024) uses MDCM to capture object features in frequency and spatial domains across times, and MFGatt to reduce style impact, focusing on object location. JFRNet (Chang et al., 2024) introduces a three-branch network that takes joint bi-temporal features as unified input, enabling each branch to perceive the semantic relevance of the two time points without any additional interaction operations. DecoderFusion (Li et al., 2024) enhances CD decoding features by leveraging the feature differences between two semantic segmentation decoding branches. CdSC (Wang et al., 2024) introduces a cross-differential semantic consistency network that explores the differences in bi-temporal features while maintaining their semantic consistency. HGINet (Long et al., 2024) builds a multi-level perception aggregation network with a pyramid architecture to extract features that distinguish different categories across multiple levels. How-

ever, these methods only consider single-modal data, i.e., images, while neglecting the rich semantic information embedded in multimodal data, thus encountering a performance bottleneck.

2.2. Multimodal Learning

Recent studies have shown that multimodal information is beneficial for visual image analysis. LAVT (Yang et al., 2022b) and VLT (Ding et al., 2023) integrate textual features into visual features through language encoders. Zhang et al. (Zhang et al., 2023) propose a convolutional neural network method with an attention mechanism to enhance feature extraction for lidar data. Their approach leverages the elevation information from lidar data and the spatial-spectral information of hyperspectral data for multimodal feature fusion. MedCLIP (Koleilat et al., 2024) uses text prompts to generate segmentation for clinical scans, adopting a novel decoupled hard-negative noise contrastive estimation loss to fine-tune the BiomedCLIP model. ChangeCLIP (Dong et al., 2024) designs a novel CD framework that utilizes semantic information from image-text pairs and introduce an innovative differential feature compensation module to capture fine-grained semantic changes between them.

2.3. Frequency Transform in Deep Learning

In image processing, the combination of CNN and frequency domain information has been widely applied in tasks such as image restoration, super-resolution, and semantic segmentation. W-Unet (Zhao et al., 2021) replaces down-sampling operations with DWT to reduce the impact of image noise while avoiding information loss. FFT-ReLU (Mao et al., 2023) performs image deblurring tasks in the frequency domain based on fast Fourier transform. ARFFT (Zhu et al., 2023) proposes a spatial-frequency fusion block to enhance the representation capability of Transformers and extend the receptive field across the entire image. XNet (Zhou et al., 2023) utilizes wavelet transforms to transfer visual information to the frequency domain, leveraging high- and low-frequency information to design a framework supporting both fully supervised and semi-supervised tasks. Given the characteristics of RS images, such as high resolution and susceptibility to spectral variations caused by seasonal changes, using only frequency domain features of-



Figure 4: Examples of dataset distribution spanning multiple representative geographical areas.

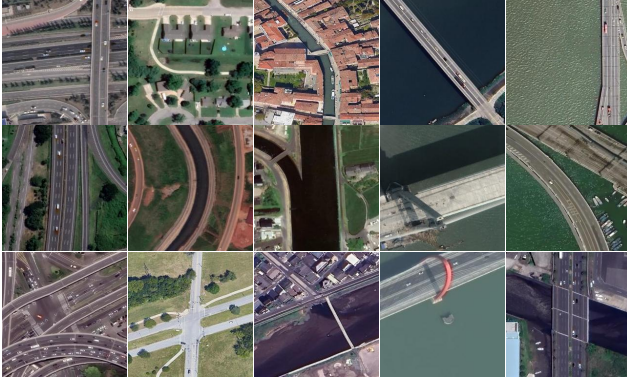


Figure 5: Examples of road and bridge types, where the first two columns are roads, and the last three columns are bridges.

ten results in the loss of critical spatial information. Therefore, in this paper, we propose a novel architecture that models multimodal features in the frequency domain, effectively balancing the advantages of visual features, textual features, and frequency domain features, achieving promising results.

3. RB-SCD Dataset

3.1. Data Annotation and Analysis

Rich Semantic Annotations: As shown in Figure 1 and Figure 3, unlike traditional BCD datasets, we have defined eight major categories (with specific subcategories detailed in Table 2), including road, bridge, bare land, building, farmland, water, grass and vegetation. The RB-SCD dataset provides detailed semantic change annotations for 11 distinct types of semantic changes and a background category across these eight categories. Changes such as road widening, new road construction, and bridge construction or modification are reflected through the corresponding semantic change types, supporting in-depth exploration of the intrinsic mechanisms of traffic scenario evolution. It is worth

noting that some changes, such as bridges directly turning into roads, are rarely observed in reality. Additionally, other types of changes, such as those between bridges and some other categories, occur in only a few samples, and we set their pixel number to 0. All annotations are carried out by a professional team in RS and transportation, and underwent multiple rounds of rigorous review and quality control to ensure annotation accuracy and semantic consistency.

Diverse Geographic Coverage: As shown in Figure 4, following the principles in (Long et al., 2021), we collect 260 pairs of RS images with resolutions ranging from 270×534 to $7,215 \times 4,366$ (0.59 m/pixel), which can be cropped into 5,016 pairs of 256×256 patches, including 4,015 pairs for the training set and 1,001 pairs for the testing set. The dataset integrates satellite images obtained primarily from Google Earth, covering various regions worldwide, including Chinese cities such as Hefei, Xi'an, Chongqing and Guangzhou, as well as representative areas from Japan, Singapore, Nigeria, Italy, America, and Indonesia, etc. This extensive geographic coverage ensures that the dataset encompasses traffic scenes under varying climatic conditions, geological structures, and urban planning contexts, thereby guaranteeing its diversity and representativeness.

Multiple Road and Bridge Types: As shown in Figure 5, the dataset encompasses various types of roads and bridges from different geographical regions and urban environments. The road categories include concrete and asphalt roads used for urban main roads, secondary roads, residential streets, and highways, comprehensively reflecting the common transportation routes found in cities. Additionally, the dataset contains elevated roads designed to alleviate congestion and improve traffic efficiency, which are typically found in densely populated or high-traffic urban areas. In terms of bridge structures, the dataset includes large cable-stayed bridges that span wide rivers or deep valleys, as well as girder bridges and pedestrian bridges used for

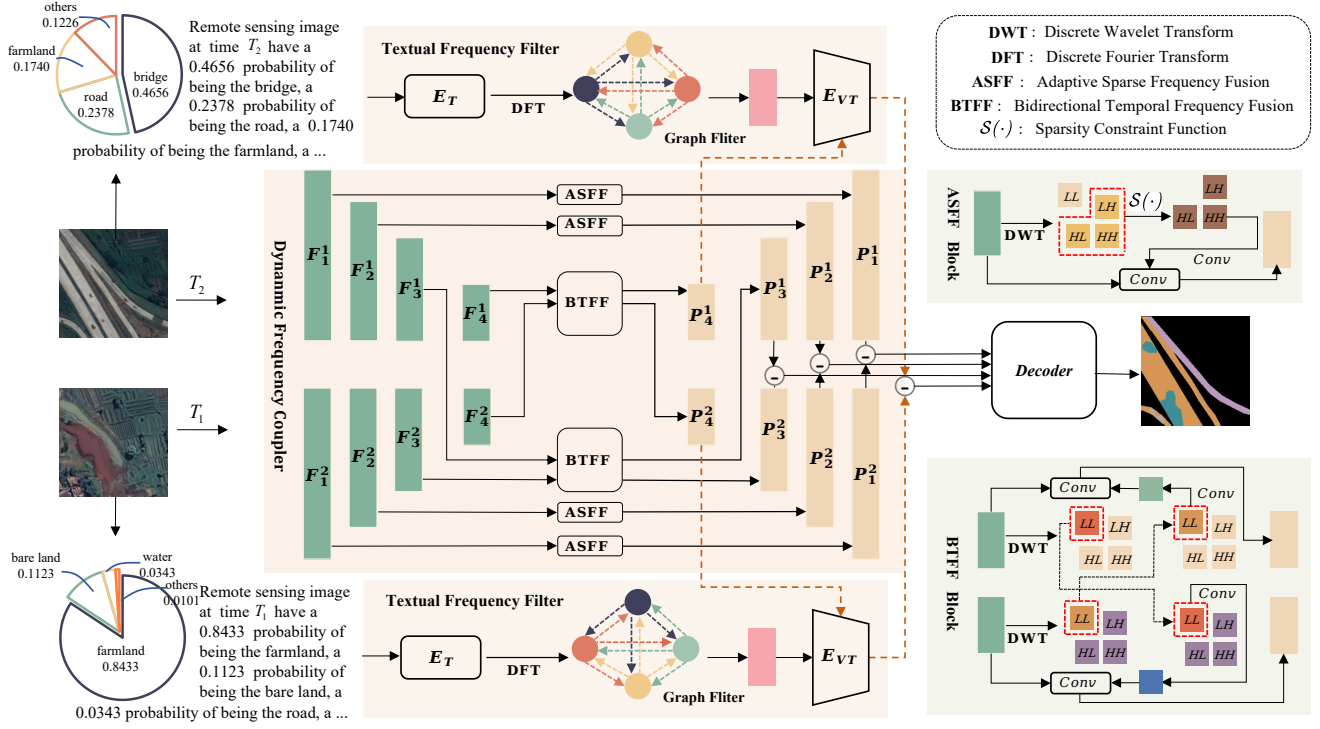


Figure 6: Overview of our proposed Multimodal Frequency-Driven Change Detector (MFDCD).

short- to medium-span connections and pedestrian access. The dataset also includes other types of specialized roads and bridges, demonstrating a variety of engineering styles and applications. This richness in road and bridge types enables the dataset to represent complex traffic environments and provides robust support for training CD models across multiple scales and diverse scenarios.

3.2. Label Imbalance Analysis and Challenges

As shown in Figure 3, our RB-SCD dataset exhibits a certain degree of sample imbalance, primarily manifested in the unequal distribution of different road and bridge types as well as change categories. Due to the diversity in data collection times and geographical regions, some categories of roads, bridges, and change types have fewer samples. In terms of semantic changes, there is also an imbalance in the types of changes in the dataset, especially for fine-grained CD tasks. For some types of changes (e.g., road widening, bridge construction), there are more samples, while for other types of changes (e.g., road repair, demolition), there are fewer samples. This imbalance may lead to the model overfitting to the more common change types, while neglecting the rarer ones. Additionally, the imbalance between change and no-change samples is another issue, particularly for CD tasks. The no-change samples are relatively more abundant, which may lead to a decrease in the model's sensitivity when processing change samples. To improve the accuracy and robustness of the model, we will further collect more samples of different types of changes in future work and employ techniques such as data augmentation and sample weighting to alleviate the model's difficulty in detecting rare changes.

4. Methodology

4.1. Overview

As shown in Figure 6, our MFDCD mainly includes two components: (1) DFC module effectively couples high-level and low-level visual features with high-frequency and low-frequency spectral features. (2) TFF module enhances the text information obtained through zero-shot inference, explores the representation of text features in the frequency domain, and promotes the interaction and fusion of multimodal data. The details are as follows.

4.2. DFC Module

Given the bi-temporal images T_1 and T_2 , ResNet50 (He et al., 2016) is used as the backbone network to extract the corresponding multi-scale features $F_i^t (i \in \{1, 2, 3, 4\}, t \in \{1, 2\})$. The features from the first two layers of the network are considered as low-level features, while the features from the last two layers are considered as high-level features. The low-frequency and high-frequency components of these features are then obtained through wavelet transform, which allows for the separation of coarse and fine-grained information in both spatial and frequency domains.

Adaptive Sparse Frequency Fusion: Low-level features are rich in detailed information, while high-frequency features contain information about edges, details, and abrupt changes, which naturally correspond to low-level features. However, high-frequency features are sensitive to noise and may amplify the influence of irrelevant regions. As shown in the upper-right corner of Figure 6, the ASFF block applies a novel sparsity constraint to the high-frequency features,

which is dynamically adjusted during training iterations. By combining the sparsity-constrained high-frequency features with low-level features, both the image's detailed information (such as edges and textures) and local structural information are preserved. This combination makes the network more responsive to CD, especially in areas with detailed changes. The process is as follows:

$$LL_i^t, HL_i^t, LH_i^t, HH_i^t = \mathcal{W}(F_i^t), \quad (1)$$

where $t \in \{1, 2\}$, $i \in \{1, 2, 3, 4\}$, $\mathcal{W}(\cdot)$ represents the discrete wavelet transform. LL_i^t is the low-frequency band, HL_i^t , LH_i^t , and HH_i^t signifying the high-frequency bands.

$$H_i^t = \text{Conv}(\text{Cat}(HL_i^t, LH_i^t, HH_i^t)), \quad (2)$$

$$\widetilde{H}_i^t = S(H_i^t, \lambda(p), g) = \begin{cases} H_i^t, & \text{if } |H_i^t| > g \cdot \lambda(p) \\ 0, & \text{otherwise} \end{cases}, \quad (3)$$

$$\lambda(p) = \lambda_0 \cdot e^{-\gamma p}, \quad (4)$$

$$P_i^t = \text{Conv}(\text{Cat}(Up(\widetilde{H}_i^t), F_i^t)), \quad (5)$$

where $t \in \{1, 2\}$, $i \in \{1, 2\}$. $S(\cdot)$ denotes the sparsity constraint function, which is used to apply the sparsity operation, $\lambda(p)$ is the dynamic sparsity strength, λ_0 is the initial sparsity strength, γ is the sparsity decay rate, p is the current training iteration, and g is a constant controlling the sparsity strength. H_i^t is the original fused high-frequency feature and \widetilde{H}_i^t is the high-frequency feature after applying the sparsity constraint. P_i^t is the enhanced feature that combines high-frequency and low-level information. $\text{Conv}(\cdot)$ and $Up(\cdot)$ are convolution and bilinear upsampling operation, respectively.

Bidirectional Temporal Frequency Fusion: As shown in the lower-right corner of Figure 6. Take the low-frequency features of time T_2 and the high-level features of time T_1 as an example, high-level features at time T_1 typically contain the semantic hierarchy of the image, enabling the expression of global structural changes in the image, such as road widening and bridge construction. Low-frequency features at time T_2 mainly focus on smooth regions or large-scale change information in the image. By combining high-level features from T_1 with low-frequency features from T_2 , the network can capture global structural changes across time points while maintaining sensitivity to large-scale, smooth region changes. This models the bidirectional relationship of changes: local changes at T_1 may lead to semantic-level changes at T_2 , while detailed changes at T_2 may arise from regional distribution adjustments at T_1 . The details of BTFF block are as follows:

$$P_i^1 = \text{Conv}(\text{Cat}(Up(LL_i^2), F_i^1)), \quad (6)$$

$$P_i^2 = \text{Conv}(\text{Cat}(Up(LL_i^1), F_i^2)), \quad (7)$$

where $i \in \{3, 4\}$, P_i^t is the enhanced feature that combines low-frequency information and high-level information.

4.3. TFF Module

As shown in Figure 6, we leverage the powerful zero-shot inference capability of the CLIP model to obtain textual information from RS images for multimodal modeling. For the categories inferred by the CLIP model, we select the top five categories with the highest probability values. For the foreground features, the text description T_d is designed in the format "Remote sensing image at time $\{period\}$ has a $\{value\}$ probability of being the $\{key\}$," where $\{period\}$ represents either T_1 or T_2 , $\{value\}$ is the probability value of the corresponding category and $\{key\}$ represents the category itself. E_T is a pre-trained CLIP text encoder that encodes the text embedding. Considering that discrete Fourier transform can help to reveal high-order semantic patterns in text, especially by identifying more complex semantic information through the descriptors used at different temporal points (T_1 , T_2). Through Fourier transform, periodic or repetitive structures in the text can be extracted, which helps identify commonalities and differences in changes. We first use Fourier transform to convert the text embeddings from the text domain to the frequency domain:

$$\mathbf{T}_{freq} = \mathcal{F}(E_T(T_d)), \quad (8)$$

where $\mathcal{F}(\cdot)$ is the discrete Fourier transform, $\mathbf{T}_{freq} \in \mathbb{C}^{B \times N \times C}$, B represents the batch size, N represents the number of frequency components, C represents the dimension of each frequency component. We introduce a graph filter bank $\mathbf{K} = [k_1, k_2, \dots, k_k]$ for the textual features, which propagate information between the nodes of the graph to filter and refine the frequency information, thereby obtaining salient features related to the changes. For the frequency feature \mathbf{T}_{freq} , we split it into real and imaginary parts and concatenate them to construct node features. The feature matrix $\mathbf{X} \in \mathbb{R}^{B \times N \times 2C}$ is the collection of features for all nodes, which allows us to convert frequency domain information into node features for the graph. Assuming that each frequency component is connected to every other frequency component (fully connected graph), the edge set $\mathbf{E} \in \mathbb{Z}^{2 \times \frac{N(N-1)}{2}}$ of the graph can be constructed by combining each pair of nodes:

$$\mathbf{X} = \text{Cat}[\Re(\mathbf{T}_{freq}), \Im(\mathbf{T}_{freq})], \quad (9)$$

$$\mathbf{E} = \{(i, j) \mid 1 \leq i \neq j \leq N\}, \quad (10)$$

$$\mathbf{E}^{(k+1)} = \sigma(\hat{\mathbf{A}}\mathbf{E}^{(k)}\mathbf{W}_k), \quad (11)$$

$$\mathbf{E}^f = \sum_{k=1} \mathbf{E}^{(k)}, \quad (12)$$

where $\Re(\mathbf{T}_{freq})$ and $\Im(\mathbf{T}_{freq})$ represent the real and imaginary parts of the frequency domain features, respectively. $\mathbf{E}^{(k)}$ represents the node features after the k -th filter, $\hat{\mathbf{A}}$ is the normalized adjacency matrix, which represents the relationships between nodes, \mathbf{W}_k is the weight matrix of the graph convolution filter at the k -th layer, and σ is the activation function, \mathbf{E}^f is the weighted sum of the outputs from multiple filters. We use the text-image encoder E_{VT} of the CLIP model to fuse \mathbf{E}^f and the image features. After subtracting the results from the bi-temporal phases, the output is fed into the decoder (Chen et al., 2024) to obtain our CD results.

Table 3

Public CD datasets used in the experiments.

Datasets	Train/ Val/ Test	Image type	Space resolution
LEVIR-CD	7120/ 1024/ 2048	Satellite images	0.5 m/pixel
SYSU-CD	12000/ 40000/ 4000	Aerial images	0.5 m/pixel
WHU-CD	5947/ 743/ 744	Aerial images	0.2 m/pixel

4.4. Frequency Transform Function Analysis

Why use discrete wavelet transform for image features and discrete Fourier transform for textual features? The advantage of wavelet transform lies in its ability to analyze images at different scales and locations, making it particularly suitable for multi-level, multi-scale image analysis tasks. As shown in Figure 2, in remote sensing image CD, wavelet transform helps to extract high-frequency features (e.g., detailed changes) and low-frequency features (e.g., overall structure), aiding in the capture of changes at different spatiotemporal scales in the image. Considering that text is typically discrete sequential data, its changes are often global or frequency-related. Therefore, on the other hand, the Fourier transform can effectively reveal periodic semantic patterns in the text, which contributes to identify patterns and trends in text changes.

5. Experiments and Results

5.1. Public CD Datasets

In addition to using our proposed dataset, as shown in Table 3, we have employed three public CD datasets to evaluate the robustness of our model. The LEVIR-CD (Chen and Shi, 2020) dataset consists of 637 pairs of RS images with a resolution of $1,024 \times 1,024$. It mainly focuses on building area changes, such as building growth. The WHU-CD (Ji et al., 2018) dataset comprises a pair of high-resolution RS images with a size of $32,507 \times 15,354$ pixels. It covers areas before and after an earthquake and primarily includes building renovations and additions. The SYSU-CD (Shi et al., 2021) dataset is a collection of 20,000 pairs of high-resolution aerial images, each with a size of 256×256 pixels. The images are captured in the Hong Kong area and include urban construction, suburban expansion, and vegetation changes, etc.

5.2. Implementation Details

Our experiments are conducted on a single NVIDIA GeForce RTX 3090 GPU. The AdamW (Kingma and Ba, 2014) is employed, with a learning rate of 0.0001 and a weight decay parameter of 0.01. Cross entropy loss is used as our loss function, and the maximum number of iterations is set to 40,000. For data augmentation, RandomFlip and PhotoMetricDistortion are applied. The constant g in the ASFF block is set to 0.1, the decay rate γ is set to 0.0001, and λ_0 is set to 1. To evaluate the performance of our experiments, we adopt four widely used metrics: recall (Rec), precision (Pre), F1-score (F1) and intersection over union (IoU), where IoU and F1 are the primary metrics, while the

others are auxiliary metrics. The following are formulas for defining the evaluation metrics as mentioned above.

$$Rec = TP / (TP + FN), \quad (13)$$

$$Pre = TP / (TP + FP), \quad (14)$$

$$F1 = 2 / (Rec^{-1} + Pre^{-1}), \quad (15)$$

$$IoU = TP / (TP + FP + FN), \quad (16)$$

where TP, TN, FP, and FN denote the counts of true positives, true negatives, false positives, and false negatives, respectively.

5.3. Quantitative Assessment Results

Results for Semantic Change Detection on RB-SCD

Dataset: Table 4 presents the comparative results of our method and several advanced SCD methods across multiple evaluation metrics. As shown in the table, we have defined 11 types of semantic changes along with one background category, aiming to comprehensively cover the diverse real-world scenarios of road and bridge changes. These change types include both relatively straightforward categories—such as *water to bridge* and *farmland to road*, which typically involve simple backgrounds or abundant training samples—and more challenging categories, such as *road to vegetation* and *grass to road*, which are characterized by complex backgrounds, ambiguous boundaries, and limited sample sizes. Across this diverse range of semantic changes, our method achieves significant advantages in both the IoU and F1 metrics. Specifically, for the easily detectable categories—*water to bridge*, *bridge to water*, *water to road*, and *farmland to road*—our model attains IoU scores of 86.83%, 83.58%, 71.68%, and 68.40%, respectively, significantly outperforming other comparison methods. These results highlight the strong capability of our model in semantic discrimination and spatial reasoning. More importantly, our method also performs excellently on several challenging categories, including *road to vegetation*, *road to grass*, *road to bare land*, and *grass to road*, which suffer from sample scarcity and semantic ambiguity. These types of changes are often affected by similar surface textures, seasonal variability, and complex contextual information. Traditional methods are prone to false positives and missed detections under such conditions, whereas our model consistently demonstrates strong robustness and generalization ability by accurately identifying these subtle semantic transformations.

Furthermore, we evaluate the performance of the latest RS foundation model, LWGANet (Lu et al., 2025), on our proposed dataset (as shown in Table 5). The results further underscore the challenging nature of our dataset. By incorporating fine-grained and practically meaningful semantic change categories in traffic scenarios, our dataset provides a more rigorous and instructive benchmark for training and evaluating CD models in real-world applications.

Results for Binary Change Detection on RB-SCD

Dataset: As shown in Table 6, in the BCD task based on the RB-SCD dataset, different models exhibit varying

Table 4

Comparison of quantitative performance for semantic change detection on RB-SCD dataset. All metrics are expressed as percentages (%). Results highlighted in **red** indicate the best performance, while those in **blue** denote the second-best performance.

Class	HGINet (Long et al., 2024)				CdSC (Wang et al., 2024)				DEFO (Li et al., 2024)				ChangeCLIP (Dong et al., 2024)				Ours			
	IoU	F1	Rec	Pre	IoU	F1	Rec	Pre	IoU	F1	Rec	Pre	IoU	F1	Rec	Pre	IoU	F1	Rec	Pre
background	97.76	98.87	99.14	98.60	98.22	99.10	99.45	98.75	98.18	99.08	98.27	98.90	98.11	99.05	99.37	98.73	98.28	99.13	99.34	98.93
bare land -> road	45.24	62.30	61.10	63.54	48.42	65.25	63.40	67.21	50.93	67.49	66.04	69.00	51.75	68.21	64.87	64.87	52.76	69.08	69.49	68.67
water -> bridge	80.20	89.01	85.60	92.71	85.33	92.09	93.32	90.88	83.10	90.77	91.38	90.17	85.77	92.34	88.22	96.87	86.83	92.95	94.28	91.67
water -> road	58.09	73.49	76.88	70.39	68.64	81.49	74.82	89.26	62.78	77.14	76.21	78.88	68.11	81.03	76.23	86.47	71.68	83.51	79.63	87.78
road -> bare land	33.83	50.55	40.13	68.29	38.33	55.42	44.58	73.22	38.14	55.22	48.02	64.94	40.57	57.72	47.06	74.63	39.48	56.61	43.88	79.73
road -> vegetation	10.69	19.32	12.56	41.82	13.65	24.03	15.25	56.57	17.02	29.09	22.47	41.25	16.37	28.13	19.35	51.49	20.31	33.76	21.83	74.39
vegetation -> road	52.61	68.94	63.10	75.98	57.93	73.36	69.89	77.19	57.84	73.29	72.30	74.41	57.10	72.69	68.55	77.37	59.35	74.49	72.38	76.72
building -> road	36.56	55.57	43.44	69.78	36.10	53.05	41.28	74.18	39.83	56.97	51.63	63.54	40.46	57.61	44.69	81.04	45.44	62.49	53.06	75.98
farmland -> road	63.36	73.55	77.80	77.34	63.80	77.90	78.78	86.61	65.38	79.07	75.87	82.55	65.02	78.80	81.30	76.45	68.40	81.24	79.21	83.38
grass -> road	36.55	53.54	39.09	84.94	36.66	53.65	46.45	64.48	40.60	57.75	48.26	71.89	36.55	53.54	39.09	84.94	42.49	59.64	47.24	80.86
road -> grass	22.44	36.65	32.38	42.21	15.53	26.89	17.41	58.97	18.41	31.10	22.75	49.14	21.76	35.75	24.21	68.26	21.65	35.59	22.86	80.30
bridge -> water	46.51	63.49	49.92	87.19	79.36	82.60	74.25	93.06	83.40	90.95	93.45	88.57	77.86	87.55	90.44	84.85	83.58	91.05	90.34	91.78
mIoU	48.65				52.75				54.63				54.95				57.52			

Table 5

Performance of the RS foundation model LWGNet on RB-SCD dataset. All metrics are expressed as percentages (%).

Class	LWGNet-L1 (Lu et al., 2025)				LWGNet-L2 (Lu et al., 2025)			
	IoU	F1	Pre	Rec	IoU	F1	Pre	Rec
background	98.3	99.14	98.84	99.44	98.27	99.13	98.8	99.45
bare land -> road	54.17	70.27	73.28	67.5	53.17	69.42	74.46	65.02
water -> bridge	87.29	93.21	92.52	93.92	85.85	92.39	90.95	93.87
water -> road	69.53	82.03	82.51	81.55	63.42	77.62	83.84	72.25
road -> bare land	38.54	55.64	78.94	42.95	38.06	55.14	74.67	43.71
road -> vegetation	15.54	26.89	55.44	17.75	13.7	24.1	68.9	14.6
vegetation -> road	59.14	74.32	75.55	73.13	60.1	75.08	78.81	71.68
building -> road	42.1	59.25	81.97	46.4	42.27	59.42	76.5	48.57
farmland -> road	69.94	82.31	86.16	78.79	71.04	83.07	83.96	82.2
grass -> road	28.98	44.93	81.75	30.98	40.78	57.93	81.93	44.81
road -> grass	22.78	37.11	83.44	23.86	21.87	35.89	84.47	22.79
bridge -> water	75.1	85.78	89.44	82.41	80.01	88.9	89.56	88.24
mIoU	55.12				55.71			

Table 6

Comparison of quantitative performance for binary change detection on RB-SCD dataset. All metrics are expressed as percentages (%). Results highlighted in **red** indicate the best performance, while those in **blue** denote the second-best performance.

Model	IoU	F1	Rec	Pre
FC-diff (Caye Daudt et al., 2018)	57.81	73.26	69.63	77.30
FC-ef (Caye Daudt et al., 2018)	59.05	74.26	69.05	80.31
FC-cat (Caye Daudt et al., 2018)	60.34	75.26	71.99	78.85
SNUNet (Fang et al., 2022)	62.90	77.22	72.47	82.64
BIT (Chen et al., 2022)	62.21	76.71	70.97	83.69
ChangeFormer (Bandara and Patel, 2022)	61.88	76.45	69.69	84.66
ICIF (Feng et al., 2022)	61.80	76.39	71.93	81.43
TFL-GR (Li et al., 2022)	64.72	78.58	73.78	84.05
DMINet (Feng et al., 2023)	62.99	77.29	72.14	83.24
USSFC-Net (Lei et al., 2023)	62.55	76.96	75.07	78.95
ELGC-Net (Noman et al., 2024)	65.53	79.18	73.99	85.15
Ours	65.83	79.39	74.13	85.47

performance across different evaluation metrics. In terms of the IoU metric, our model ranks first with a score of 65.83%, slightly outperforming ELGC-Net (Noman et al., 2024), which achieves 65.53%. This indicates that MFDCD demonstrates the best performance in terms of overlap between the predicted and ground truth change regions, enabling more precise localization of change areas. Regarding the F1, our MFDCD model also leads with a score of 79.39%, followed closely by ELGC-Net at 79.18%. Since the F1 is a harmonic mean of Pre and Rec, this result sug-

gests that MFDCD achieves an excellent balance between detection accuracy and completeness. For recall, USSFC-Net (Lei et al., 2023) achieves the highest score of 75.07% among all models, while our model follows closely with a recall of 74.13%, ranking second. This demonstrates that USSFC-Net has a strong ability to detect all change areas, and our model also exhibits competitive performance in capturing changed regions. In terms of precision, our model outperforms others with a score of 85.47%, while ELGC-Net follows at 85.15%. This implies that our model has a lower false positive rate when identifying change areas. Overall, the results of the BCD task further indicate that existing methods still have room for improvement when applied to our RB-SCD dataset.

Results on Public CD Datasets: To further prove the validity of our model, we also compare our proposed MFDCD with thirteen state-of-the-art CD techniques. To ensure a fair comparison, we reproduce these methods using publicly available code with default parameters. Table 7 presents the quantitative evaluations of various methods on three public CD datasets, including IoU, F1, Rec, and Pre metrics. As observed in Table 7, our method achieves outstanding results across all three publicly available datasets. Specifically, on the WHU-CD dataset, our approach outperforms the second-best method by 2.69% and 1.5% in IoU and F1, respectively. On the SYSU-CD dataset, it achieves improvements of 4.43% and 3.05%, while on the LEVIR-CD dataset, it surpasses the second-best method by 1.06% and 0.62%. These results further demonstrate the effectiveness and robustness of our method.

5.4. Quantitative Analysis.

As shown in Figure 7, we compared the visualized results of the proposed MFDCD with other state-of-the-art methods on RB-SCD dataset. From the figure, it can be observed that our method outperforms others in identifying small semantic change regions. For instance, as shown in the third row, our method better distinguishes between changes from grass to road and from vegetation to road—two types of changes with similar characteristics. Regarding pseudo-changes caused by background composition, such as in the fifth row, where a boat passing under a bridge with its bow

Table 7

Comparison of quantitative performance of various CD techniques on public datasets. All metrics are expressed as percentages (%). Results highlighted in **red** indicate the best performance, while those in **blue** denote the second-best performance. Results marked with * are obtained from the original papers.

Model	LEVIR-CD (Chen and Shi, 2020)				SYSU-CD (Shi et al., 2021)				WHU-CD (Ji et al., 2018)			
	IoU	F1	Rec	Pre	IoU	F1	Rec	Pre	IoU	F1	Rec	Pre
FC-diff (Caye Daudt et al., 2018)	75.18	85.83	84.59	87.12	42.05	59.20	46.72	80.80	69.48	81.99	78.90	89.14
FC-ef (Caye Daudt et al., 2018)	71.80	83.59	82.27	84.94	55.83	71.65	65.41	79.22	58.53	71.65	65.41	79.22
FC-cat (Caye Daudt et al., 2018)	76.98	86.99	85.64	88.38	60.68	75.53	71.38	80.21	72.24	83.87	84.22	83.53
SNUNet (Fang et al., 2022)	82.20	90.23	88.97	91.54	66.73	80.04	79.79	80.30	76.02	86.38	88.95	83.95
BIT (Chen et al., 2022)	82.06	90.15	88.98	91.34	62.50	76.93	72.50	81.93	80.40	89.13	89.69	88.58
ChangeFormer (Bandara and Patel, 2022)	81.93	90.07	87.38	92.92	60.46	75.36	71.06	80.22	83.88	91.23	90.76	91.71
ICIF (Feng et al., 2022)	79.86	88.80	86.85	90.84	61.38	76.07	73.31	91.94	78.27	87.81	84.06	91.96
TFI-GR (Li et al., 2022)	83.03	90.73	89.53	91.95	71.38	83.30	81.16	85.56	88.55	93.92	92.65	95.24
DMINet (Feng et al., 2023)	83.14	90.79	88.89	92.78	68.20	81.10	76.82	85.88	79.53	88.60	91.24	86.10
USSFC-Net (Lei et al., 2023)	82.54	90.44	91.82	89.09	65.75	79.34	81.52	77.27	83.92	91.26	93.20	89.40
M-Swin* (Pan et al., 2024)	83.57	91.05	90.05	92.07	-	-	-	-	86.09	92.94	91.37	94.56
ELGC-Net (Noman et al., 2024)	83.52	91.02	89.78	92.30	65.34	79.03	77.26	80.89	75.56	86.08	82.15	90.40
MDENet* (Liu et al., 2024)	83.63	91.09	92.68	89.55	-	-	-	-	87.74	93.47	95.49	91.54
Ours	84.69	91.71	92.31	91.11	72.63	84.15	85.60	82.74	90.43	94.97	96.44	93.55

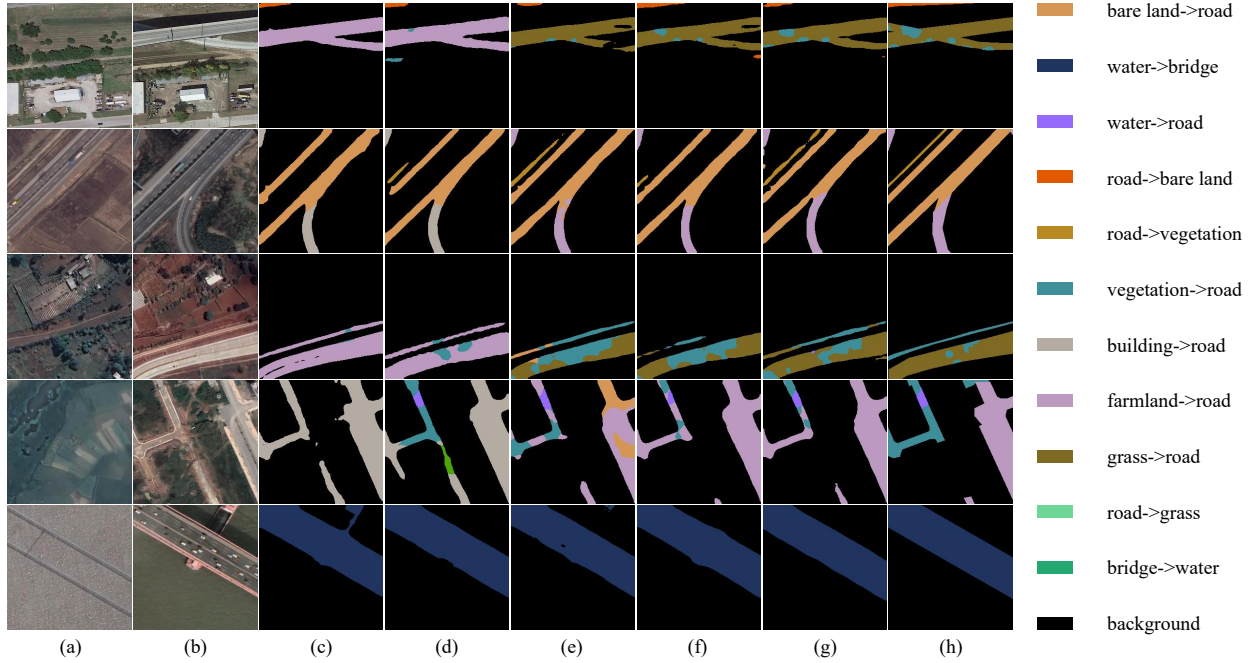


Figure 7: Qualitative visualization for semantic change detection on RB-SCD dataset. (a) T_1 images. (b) T_2 images. (c) HGINet. (d) CdSC. (e) DEFO. (f) ChangeCLIP. (g) Ours. (h) Label.

color similar to the bridge’s edge color, both DEFO (Li et al., 2024) and ChangeCLIP (Dong et al., 2024) made incorrect predictions, while our method accurately detected the changes. Additionally, the proposed dataset presents significant challenges. For example, in the first row, all methods struggle to detect semantic changes under road shadows. As shown in the second row, farmland in autumn and winter appears visually similar to bare land, and in the fourth row, farmland in spring and summer shares similar colors with water, resulting in low inter-class differences. In such challenging scenes, other methods show many false detections, while our method performs slightly better but still leaves room for improvement.

When comparing the BCD results of each method with

the ground truth in Figure 8, it can be observed that for the unchanged areas (black regions representing true negatives), most models show relatively accurate results, with fewer false positives. In contrast, for the changed areas, the performance varies among models. Some models exhibit noticeable missed detections (blue regions representing false negatives), indicating they fail to identify all actual changes. Many models are capable of detecting building-related changes, which are common in the dataset. For example, in areas where buildings are newly constructed or modified, most models can capture at least part of the change, though the precision of boundary detection varies. In regions where there is a transition from bare land to road, our MFDCD and some others show better performance in

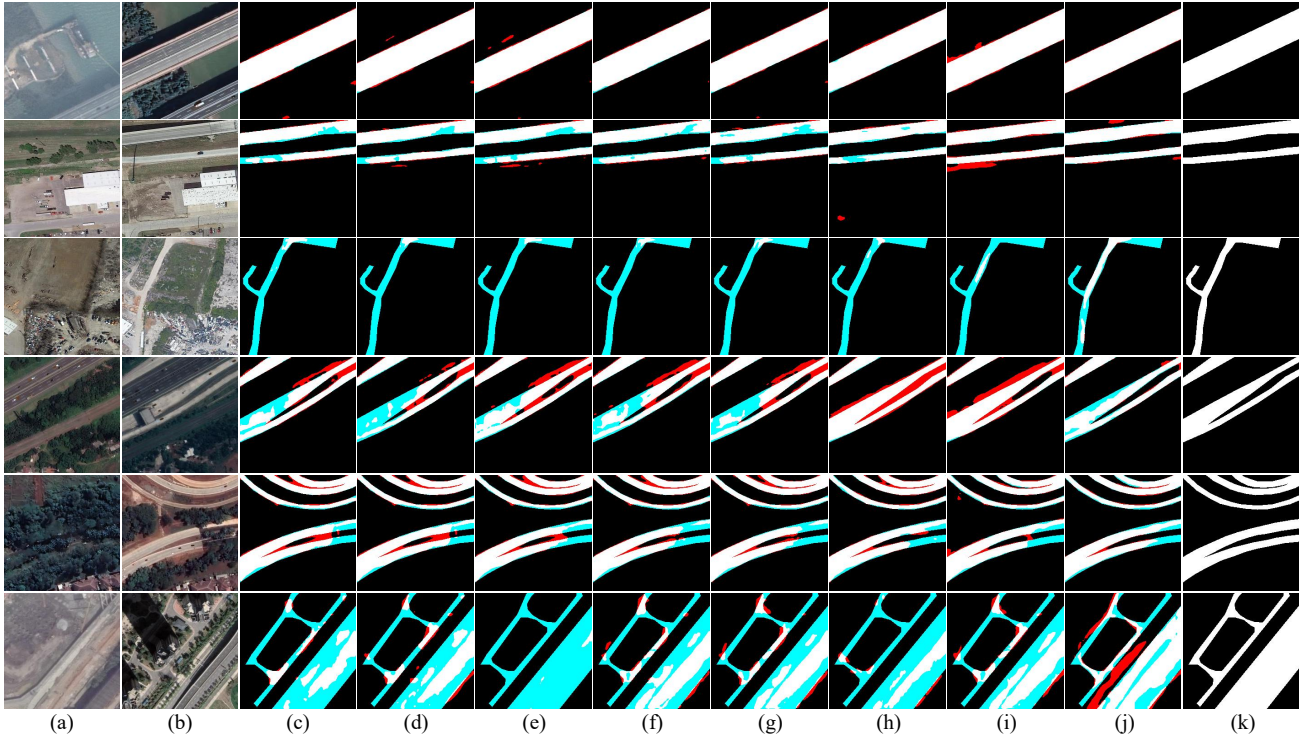


Figure 8: Qualitative visualization for binary change detection on RB-SCD dataset. (a) T_1 images. (b) T_2 images. (c) BIT. (d) ChangeFormer. (e) ICIF. (f) TFI-GR. (g) DMINet. (h) USSFC-Net. (i) ELGC-Net. (j) Ours. (k) Label. The rendered colors represent true positives (white), false positives (red), true negatives (black), and false negatives (blue).

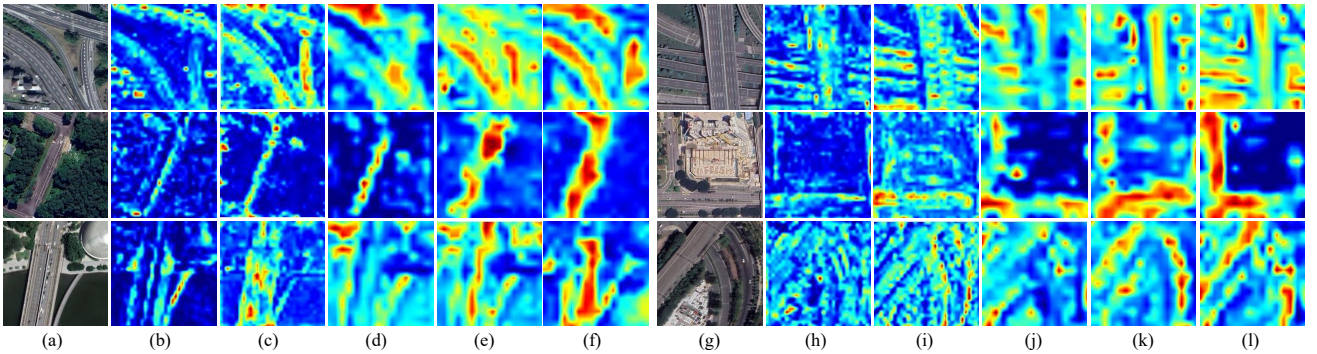


Figure 9: Heatmaps of our proposed modules. (a) and (g) Input images. (b) and (h) Low-level features from the backbone network. (c) and (i) High-level features from the backbone network. (d) and (j) Feature maps after undergoing the ASFF block. (e) and (k) Feature maps after undergoing the BTFF block. (f) and (l) Feature maps after undergoing the TFF module.

accurately delineating the change area. Some methods, however, have varying degrees of missed detections. For instance, methods such as BIT (Chen et al., 2022) and ChangeFormer (Bandara and Patel, 2022) seem to have less accurate delineation compared to our method and ELGC-Net (Noman et al., 2024). In areas where buildings are under construction in one image and completed in another, different models have different performances. Some models, like ICIF (Feng et al., 2022) and TFI-GR (Li et al., 2022), can detect the change but with somewhat blurred boundaries compared to the ground truth (white regions representing true positives). Other models may miss parts of the change. In areas where the change from bare land to road is affected by shadows (resulting in pseudo-changes), most models struggle. Except

for our MFDCD, which shows relatively better performance in distinguishing true changes from pseudo-changes caused by shadows, other models either misclassify the shadow areas as changes (false positives in red) or miss the actual changes (false negatives in blue).

5.5. Ablation Study

To demonstrate the effectiveness of our proposed modules, we conduct extensive experiments on RB-SCD and three public datasets. As shown in Table 8, when the DFC module and TFF module are added to the baseline model, the mIoU on RB-SCD dataset increased by 5.44% and 4.78%, respectively. Additionally, the IoU on the LEVIR-CD, SYSU-CD, and WHU-CD datasets improved by 1.6%/2.12%/2.63%

Table 8

Ablation studies of DFC and TFF when trained on RB-SCD and public CD datasets. All values are reported as percentages (%). Results highlighted in **red** indicate the best performance, while those in **blue** denote the second-best performance.

Method	DFC	TFF	RB-SCD	LEVIR -CD	SYSU -CD	WHU -CD
(a)	×	×	50.45	81.65	68.98	86.65
(b)	✓	×	55.89	83.25	71.10	89.28
(c)	×	✓	55.23	82.97	70.89	88.50
(d)	✓	✓	57.52	84.69	72.63	90.43

Table 9

Effectiveness of the DFC module when trained on RB-SCD and public CD datasets. All values are reported in percentage (%). Results highlighted in **red** indicate the best performance, while those in **blue** denote the second-best performance.

Method	RB-SCD	LEVIR -CD	SYSU -CD	WHU -CD	
(a)	-	55.23	82.97	70.89	88.50
(b)	$F_i^1 + H_i^2, i \in \{1, 2, 3, 4\}$	55.84	83.52	71.42	89.34
(c)	$F_i^1 + LL_i^2, i \in \{1, 2, 3, 4\}$	56.10	83.67	71.68	89.45
(d)	$F_i^1 + H_i^2, F_i^2 + H_i^1, i \in \{1, 2\}$	55.70	83.39	71.23	88.90
(e)	$F_i^1 + LL_i^2, i \in \{3, 4\}$	55.86	83.51	71.30	89.24
(f)	ASFF	56.42	84.02	72.06	89.98
(g)	BTFF	56.87	83.90	71.85	89.77
(h)	ASFF+BTFF	57.52	84.69	72.63	90.43

Table 10

Effectiveness of graph filters with different numbers k in TFF. All values are reported in percentage (%). Results highlighted in **red** indicate the best performance, while those in **blue** denote the second-best performance.

Method	k	RB-SCD	LEVIR-CD	SYSU-CD	WHU-CD
(a)	-	55.89	83.25	71.10	89.28
(b)	3	56.74	83.84	71.98	89.87
(c)	4	57.13	84.13	72.31	90.10
(d)	5	57.52	84.69	72.63	90.43
(e)	6	57.40	84.26	72.25	90.38

and 1.32%/1.91%/1.85%, respectively. As shown in Table 9, we conduct detailed ablation studies on the ASFF and BTFF blocks in the DFC module. Initially, we experiment with different coupling methods for ordinary features and frequency domain features. By comparing rows (b) and (c) with row (h), we can observe that ASFF and BTFF effectively dynamically couple visual features with frequency domain features, achieving the best results. Comparing rows (d) and (f), it can be seen that combining the low-level features at time T_1 with the corresponding high-frequency features at time T_2 , due to semantic mismatches, results in worse performance compared to our designed ASFF. Comparing rows (e) and (g), it is clear that our designed BTFF captures the global structural changes across time, outperforming the coupling of high-level features and low-frequency features at the same time point. As shown in Table 10, we conduct ablation experiments on the number of layers in the frequency filter of TFF. As the value of k increased, the model’s perfor-

mance improved. However, when the number of filter layers reached six, the performance stabilized or slightly declined. Subsequent experiments are based on the optimal setting, $k = 5$. To further demonstrate the effectiveness of our modules, we visualized the intermediate layer features of the network as heatmaps. As shown in Figure 9, the proposed modules effectively enhance the detection capability for roads and bridges.

6. Conclusion

In this work, we introduce RB-SCD dataset, a SCD dataset specifically designed for complex traffic scenarios. The dataset features fine-grained pixel-level annotations across 11 semantic change categories and one background class, encompassing a wide range of road and bridge types. It also covers diverse geographic regions across multiple countries and urban environments, making it become a comprehensive and challenging benchmarks to date for road and bridge change analysis in RS imagery. Notably, RB-SCD supports both BCD and SCD tasks, offering flexibility for different application scenarios. By incorporating both common and rare semantic transformations, RB-SCD provides a valuable resource for the development and evaluation of CD models in real-world, high-density traffic contexts.

To address the unique challenges presented by this dataset, we propose a novel multimodal CD framework, MFDCD, which leverages both spatial and frequency domain representations to enhance feature learning. By introducing frequency-domain analysis into the CD pipeline, MFDCD captures subtle semantic differences and structural changes that may be overlooked by conventional spatial-domain approaches. Our method also incorporates an effective fusion mechanism to integrate multimodal features, enabling more accurate detection of complex changes such as occluded road regions. Extensive experiments conducted on the RB-SCD dataset and public CD datasets demonstrate the superior performance of MFDCD across various metrics when compared to state-of-the-art CD methods. The results highlight the robustness, generalization ability, and semantic discrimination power of our approach in both straightforward and highly ambiguous change scenarios.

In future work, we plan to extend our exploration of road and bridge change detection by integrating additional modalities such as elevation data or temporal sequences, and further investigating the role of frequency-domain representations in improving the interpretability and adaptability of CD models. As the label imbalance analysis and challenges for RB-SCD dataset discussed in Section 3.2, we also plan to expand the scale of the dataset and enrich it with more detailed spatiotemporal annotations to support broader research tasks such as urban infrastructure evolution and intelligent transportation systems. Furthermore, while MFDCD achieves strong performance, it is not yet lightweight enough for deployment in resource-constrained environments. Future research will focus on model compression and efficient architecture design to improve its applicability in real-time

and edge scenarios.

CRediT authorship contribution statement

Qingling Shu: Writing—review & editing, Writing—original draft, Methodology, Funding acquisition, Formal analysis, Data curation. **Sibao Chen:** Software, Resources, Project administration. **Zhihui You:** Validation, Supervision. **Wei Lu:** Validation, Supervision. **Jin Tang:** Validation, Supervision. **Bin Luo:** Validation, Supervision.

Declaration of competing interest

The authors declare that they have no known competing financial interests or personal relationships that could have appeared to influence the work reported in this paper.

Acknowledgement

This work was supported in part by NSFC Key Project of International (Regional) Cooperation and Exchanges (No. 61860206004), NSFC Key Project of Joint Fund for Enterprise Innovation and Development (No. U20B2068, U24A20342) and National Natural Science Foundation of China (No. 61976004).

References

- Adriano, B., Yokoya, N., Xia, J., Miura, H., Liu, W., Mat-suoka, M., Koshimura, S., 2021. Learning from multimodal and multitemporal earth observation data for building damage mapping. *ISPRS Journal of Photogrammetry and Remote Sensing* 175, 132–143. URL: <https://www.sciencedirect.com/science/article/pii/S0924271621000575>, doi:<https://doi.org/10.1016/j.isprsjprs.2021.02.016>.
- Bandara, W.G.C., Patel, V.M., 2022. A transformer-based siamese network for change detection, in: *IGARSS 2022 - 2022 IEEE International Geoscience and Remote Sensing Symposium*, pp. 207–210. doi:[10.1109/IGARSS46834.2022.9883686](https://doi.org/10.1109/IGARSS46834.2022.9883686).
- Bourdis, N., Marraud, D., Sahbi, H., 2011. Constrained optical flow for aerial image change detection, in: *2011 IEEE International Geoscience and Remote Sensing Symposium*, pp. 4176–4179. doi:[10.1109/IGARSS.2011.6050150](https://doi.org/10.1109/IGARSS.2011.6050150).
- Caye Daudt, R., Le Saux, B., Boulch, A., 2018. Fully convolutional siamese networks for change detection, in: *2018 25th IEEE International Conference on Image Processing (ICIP)*, pp. 4063–4067. doi:[10.1109/ICIP.2018.8451652](https://doi.org/10.1109/ICIP.2018.8451652).
- Caye Daudt, R., Le Saux, B., Boulch, A., Gousseau, Y., 2019. Multitask learning for large-scale semantic change detection. *Computer Vision and Image Understanding* 187, 102783. URL: <https://www.sciencedirect.com/science/article/pii/S1077314219300992>, doi:<https://doi.org/10.1016/j.cviu.2019.07.003>.
- Chang, H., Wang, P., Diao, W., Xu, G., Sun, X., 2024. A triple-branch hybrid attention network with bitemporal feature joint refinement for remote-sensing image semantic change detection. *IEEE Transactions on Geoscience and Remote Sensing* 62, 1–16. doi:[10.1109/TGRS.2024.3376384](https://doi.org/10.1109/TGRS.2024.3376384).
- Chen, H., Qi, Z., Shi, Z., 2022. Remote sensing image change detection with transformers. *IEEE Transactions on Geoscience and Remote Sensing* 60, 1–14. doi:[10.1109/TGRS.2021.3095166](https://doi.org/10.1109/TGRS.2021.3095166).
- Chen, H., Shi, Z., 2020. A spatial-temporal attention-based method and a new dataset for remote sensing image change detection. *Remote Sensing* 12, 1662.
- Chen, L., Fu, Y., Gu, L., Yan, C., Harada, T., Huang, G., 2024. Frequency-aware feature fusion for dense image prediction. *IEEE Transactions on Pattern Analysis and Machine Intelligence* 46, 10763–10780. doi:[10.1109/TPAMI.2024.3449959](https://doi.org/10.1109/TPAMI.2024.3449959).
- Daudt, R.C., Le Saux, B., Boulch, A., Gousseau, Y., 2018. Urban change detection for multispectral earth observation using convolutional neural networks, in: *IGARSS 2018-2018 IEEE International Geoscience and Remote Sensing Symposium*, Ieee. pp. 2115–2118.
- Ding, H., Liu, C., Wang, S., Jiang, X., 2023. Vlt: Vision-language transformer and query generation for referring segmentation. *IEEE Trans. Pattern Anal. Mach. Intell.* 45, 7900–7916. URL: <https://doi.org/10.1109/TPAMI.2022.3217852>, doi:[10.1109/TPAMI.2022.3217852](https://doi.org/10.1109/TPAMI.2022.3217852).
- Dong, S., Wang, L., Du, B., Meng, X., 2024. Changeclip: Remote sensing change detection with multimodal vision-language representation learning. *ISPRS Journal of Photogrammetry and Remote Sensing* 208, 53–69. URL: <https://www.sciencedirect.com/science/article/pii/S0924271624000042>, doi:<https://doi.org/10.1016/j.isprsjprs.2024.01.004>.
- Fang, S., Li, K., Shao, J., Li, Z., 2022. Snunet-cd: A densely connected siamese network for change detection of vhr images. *IEEE Geoscience and Remote Sensing Letters* 19, 1–5. doi:[10.1109/LGRS.2021.3056416](https://doi.org/10.1109/LGRS.2021.3056416).
- Feng, Y., Jiang, J., Xu, H., Zheng, J., 2023. Change detection on remote sensing images using dual-branch multilevel intertemporal network. *IEEE Transactions on Geoscience and Remote Sensing* 61, 1–15. doi:[10.1109/TGRS.2023.3241257](https://doi.org/10.1109/TGRS.2023.3241257).
- Feng, Y., Xu, H., Jiang, J., Liu, H., Zheng, J., 2022. Icf-net: Intra-scale cross-interaction and inter-scale feature fusion network for bitemporal remote sensing images change detection. *IEEE Transactions on Geoscience and Remote Sensing* 60, 4410213. doi:[10.1109/TGRS.2022.3168331](https://doi.org/10.1109/TGRS.2022.3168331).
- He, K., Zhang, X., Ren, S., Sun, J., 2016. Deep residual learning for image recognition, in: *2016 IEEE Conference on Computer Vision and Pattern Recognition (CVPR)*, pp. 770–778. doi:[10.1109/CVPR.2016.90](https://doi.org/10.1109/CVPR.2016.90).
- Ji, S., Wei, S., Lu, M., 2018. Fully convolutional networks for multisource building extraction from an open aerial and satellite imagery data set. *IEEE Transactions on geoscience and remote sensing* 57, 574–586.
- K S, B., N, S., Kevala, V.D., Lal, S., 2024. Recent advances in urban expansion monitoring through deep learning-based semantic change detection techniques from satellite imagery, in: *2024 IEEE Space, Aerospace and Defence Conference (SPACE)*, pp. 169–173. doi:[10.1109/SPACE63117.2024.10668347](https://doi.org/10.1109/SPACE63117.2024.10668347).
- Kingma, D.P., Ba, J., 2014. Adam: A method for stochastic optimization. *arXiv preprint arXiv:1412.6980*.
- Koleilat, T., Asgariandehkordi, H., Rivaz, H., Xiao, Y., 2024. Medclip-sam: Bridging text and image towards universal medical image segmentation, in: Linguraru, M.G., Dou, Q., Feragen, A., Giannarou, S., Glocker, B., Lekadir, K., Schnabel, J.A. (Eds.), *Medical Image Computing and Computer Assisted Intervention – MICCAI 2024*, Springer Nature Switzerland, Cham. pp. 643–653.
- Lebedev, M., Vizilter, Y.V., Vygolov, O., Knyaz, V.A., Rubis, A.Y., 2018. Change detection in remote sensing images using conditional adversarial networks. *The International Archives of the Photogrammetry, Remote Sensing and Spatial Information Sciences* URL: <https://api.semanticscholar.org/CorpusID:57660599>.
- Leenstra, M., Marcos, D., Bovolo, F., Tuia, D., 2021. Self-supervised pre-training enhances change detection in sentinel-2 imagery, in: *Pattern Recognition. ICPR International Workshops and Challenges: Virtual Event, January 10-15, 2021, Proceedings, Part VII*, Springer. pp. 578–590.
- Lei, T., Geng, X., Ning, H., Lv, Z., Gong, M., Jin, Y., Nandi, A.K., 2023. Ultralightweight spatial-spectral feature cooperation network for change detection in remote sensing images. *IEEE Trans. Geosci. Remote. Sens.* 61, 1–14. URL: <https://doi.org/10.1109/TGRS.2023.3261273>, doi:[10.1109/TGRS.2023.3261273](https://doi.org/10.1109/TGRS.2023.3261273).
- Li, Z., Tang, C., Wang, L., Zomaya, A.Y., 2022. Remote sensing change detection via temporal feature interaction and guided refinement. *IEEE Transactions on Geoscience and Remote Sensing* 60, 1–11. doi:[10.1109/TGRS.2022.3199502](https://doi.org/10.1109/TGRS.2022.3199502).

- Li, Z., Wang, X., Fang, S., Zhao, J., Yang, S., Li, W., 2024. A decoder-focused multitask network for semantic change detection. *IEEE Transactions on Geoscience and Remote Sensing* 62, 1–15. doi:10.1109/TGRS.2024.3362728.
- Lin, Y.C., Habib, A., 2022. Semantic segmentation of bridge components and road infrastructure from mobile lidar data. *ISPRS Open Journal of Photogrammetry and Remote Sensing* 6, 100023. URL: <https://www.sciencedirect.com/science/article/pii/S266739322000126>, doi:https://doi.org/10.1016/j.ophoto.2022.100023.
- Liu, J., Li, S., Dian, R., Song, Z., Kang, X., 2024. Mdenet: Multidomain differential excavating network for remote sensing image change detection. *IEEE Transactions on Geoscience and Remote Sensing* 62, 1–11. doi:10.1109/TGRS.2024.3413677.
- Long, J., Li, M., Wang, X., Stein, A., 2024. Semantic change detection using a hierarchical semantic graph interaction network from high-resolution remote sensing images. *ISPRS Journal of Photogrammetry and Remote Sensing* 211, 318–335. URL: <https://www.sciencedirect.com/science/article/pii/S0924271624001709>, doi:https://doi.org/10.1016/j.isprsjprs.2024.04.012.
- Long, Y., Xia, G.S., Li, S., Yang, W., Yang, M.Y., Zhu, X.X., Zhang, L., Li, D., 2021. On creating benchmark dataset for aerial image interpretation: Reviews, guidances, and million-aid. *IEEE Journal of Selected Topics in Applied Earth Observations and Remote Sensing* 14, 4205–4230. doi:10.1109/JSTARS.2021.3070368.
- Lu, W., Chen, S.B., Ding, C.H.Q., Tang, J., Luo, B., 2025. Lwganet: A lightweight group attention backbone for remote sensing visual tasks. URL: <https://arxiv.org/abs/2501.10040>, arXiv:2501.10040.
- Mao, X., Liu, Y., Liu, F., Li, Q., Shen, W., Wang, Y., 2023. Intriguing findings of frequency selection for image deblurring, in: *Proceedings of the AAAI Conference on Artificial Intelligence*, pp. 1905–1913.
- Noman, M., Fiaz, M., Cholakkal, H., Khan, S.H., Khan, F.S., 2024. Elgcnnet: Efficient local-global context aggregation for remote sensing change detection. *IEEE Trans. Geosci. Remote. Sens.* 62, 1–11. URL: <https://doi.org/10.1109/TGRS.2024.3362914>, doi:10.1109/TGRS.2024.3362914.
- Pan, J., Bai, Y., Shu, Q., Zhang, Z., Hu, J., Wang, M., 2024. M-swin: Transformer-based multiscale feature fusion change detection network within cropland for remote sensing images. *IEEE Trans. Geosci. Remote. Sens.* 62, 1–16. URL: <https://doi.org/10.1109/TGRS.2024.3374421>, doi:10.1109/TGRS.2024.3374421.
- Pekel, J.F., Cottam, A., Gorelick, N., Belward, A.S., 2016. High-resolution mapping of global surface water and its long-term changes. *Nature* 540, 418–422. URL: <https://api.semanticscholar.org/CorpusID:205252568>.
- Radford, A., Kim, J.W., Hallacy, C., Ramesh, A., Goh, G., Agarwal, S., Sastry, G., Askell, A., Mishkin, P., Clark, J., Krueger, G., Sutskever, I., 2021. Learning transferable visual models from natural language supervision, in: *International Conference on Machine Learning*. URL: <https://api.semanticscholar.org/CorpusID:231591445>.
- Shi, Q., Liu, M., Li, S., Liu, X., Wang, F., Zhang, L., 2021. A deeply supervised attention metric-based network and an open aerial image dataset for remote sensing change detection. *IEEE transactions on geoscience and remote sensing* 60, 1–16.
- Song, X., Hansen, M.C., Stehman, S., Potapov, P.V., Tyukavina, A., Vermote, E.F., Townshend, J.R., 2018. Global land change from 1982 to 2016. *Nature* 560, 639 – 643. URL: <https://api.semanticscholar.org/CorpusID:51940730>.
- Tian, S., Ma, A., Zheng, Z., Zhong, Y., 2020. Hi-ucd: A large-scale dataset for urban semantic change detection in remote sensing imagery, in: *Proceedings of the NeurIPS 2020 Workshop on Machine Learning for the Developing World: Improving Resilience*. URL: <http://arxiv.org/pdf/2011.03247v7>.
- Wang, Q., Jing, W., Chi, K., Yuan, Y., 2024. Cross-difference semantic consistency network for semantic change detection. *IEEE Transactions on Geoscience and Remote Sensing* 62, 1–12. doi:10.1109/TGRS.2024.3386334.
- Wang, X., Zhao, D., Li, X., Jia, N., Guo, L., 2025. Change detection and incremental updates for multi-source road networks considering topological consistency. *ISPRS International Journal of Geo-Information* 14. URL: <https://www.mdpi.com/2220-9964/14/1/2>, doi:10.3390/ijgi14010002.
- Yang, K., Xia, G.S., Liu, Z., Du, B., Yang, W., Pelillo, M., Zhang, L., 2022a. Asymmetric siamese networks for semantic change detection in aerial images. *IEEE Transactions on Geoscience and Remote Sensing* 60, 1–18. doi:10.1109/TGRS.2021.3113912.
- Yang, Z., Wang, J., Tang, Y., Chen, K., Zhao, H., Torr, P.H., 2022b. Lavt: Language-aware vision transformer for referring image segmentation, in: *2022 IEEE/CVF Conference on Computer Vision and Pattern Recognition (CVPR)*, pp. 18134–18144. doi:10.1109/CVPR52688.2022.01762.
- Yuan, P., Zhao, Q., Zhao, X., Wang, X., Long, X., and, Y.Z., 2022. A transformer-based siamese network and an open optical dataset for semantic change detection of remote sensing images. *International Journal of Digital Earth* 15, 1506–1525. URL: <https://doi.org/10.1080/17538947.2022.2111470>, doi:10.1080/17538947.2022.2111470, arXiv:https://doi.org/10.1080/17538947.2022.2111470.
- Zhang, H., Yao, J., Ni, L., Gao, L., Huang, M., 2023. Multimodal attention-aware convolutional neural networks for classification of hyperspectral and lidar data. *IEEE Journal of Selected Topics in Applied Earth Observations and Remote Sensing* 16, 3635–3644. doi:10.1109/JSTARS.2022.3187730.
- Zhang, M., Shi, W., 2020. A feature difference convolutional neural network-based change detection method. *IEEE Transactions on Geoscience and Remote Sensing* 58, 7232–7246.
- Zhao, C., Xia, B., Chen, W., Guo, L., Du, J., Wang, T., Lei, B., 2021. Multi-scale wavelet network algorithm for pediatric echocardiographic segmentation via hierarchical feature guided fusion. *Applied Soft Computing* 107, 107386. URL: <https://www.sciencedirect.com/science/article/pii/S1568494621003094>, doi:https://doi.org/10.1016/j.asoc.2021.107386.
- Zheng, Z., Zhong, Y., Tian, S., Ma, A., Zhang, L., 2022. Change-mask: Deep multi-task encoder-transformer-decoder architecture for semantic change detection. *ISPRS Journal of Photogrammetry and Remote Sensing* 183, 228–239. URL: <https://www.sciencedirect.com/science/article/pii/S0924271621002835>, doi:https://doi.org/10.1016/j.isprsjprs.2021.10.015.
- Zhou, Y., Huang, J., Wang, C., Song, L., Yang, G., 2023. Xnet: Wavelet-based low and high frequency fusion networks for fully- and semi-supervised semantic segmentation of biomedical images, in: *2023 IEEE/CVF International Conference on Computer Vision (ICCV)*, pp. 21028–21039. doi:10.1109/ICCV51070.2023.01928.
- Zhu, Q., Li, P., Li, Q., 2023. Attention retractable frequency fusion transformer for image super resolution, in: *2023 IEEE/CVF Conference on Computer Vision and Pattern Recognition Workshops (CVPRW)*, pp. 1756–1763. doi:10.1109/CVPRW59228.2023.00176.